Light-wave manipulation of subwavelength metallic gratings by electrically controlling the surface charge distribution based on surface-plasmon excitation

Chai Hu,[1,2,3] Taige Liu,[1,2] Kewei Liu,[1,2] Zhe Wang,[1,2] Mao Ye,[1,2] Jiashuo Shi,[1,2] and Xinyu Zhang[1,2,*]

[1] *National Key Lab of Multispectral Information Intelligent Processing Technology, Huazhong University of Science and Technology, Wuhan 430074, China*

[2] *School of Automation & Artificial Intelligence, Huazhong University of Science and Technology, Wuhan 430074, China*

[3] *Innovation Institute, Huazhong University of Science and Technology, Wuhan 430074, China*

(Received 26 August 2023; revised 25 February 2024; accepted 1 March 2024; published 28 March 2024)

This paper proposes a light-wave polarization response model based on a kind of subwavelength metallic grating (SMG) by controlling the rearrangement of surface free electrons and net positive charges. The action of charging interdigital SMGs to form a capacitor-shaped architecture can be used to modulate the surface charge distribution, leading to a decrease in the transmission of the incident light waves with initial polarization orientations parallel to the long axis of the grating (parallel waves or *P* waves) and an increase in the transmission of the incident light waves with initial polarization orientations perpendicular to the long axis of the grating (vertical waves or *S* waves), thus contributing to the modulation of the polarization state of the SMGs. By using serrated-shaped sidewalls for each nanostrip in the SMGs, the surface net charges can be more efficiently pumped onto the nearest apex in a linear nanotip array to clearly enhance or suppress the penetration of *P* waves or *S* waves in a wide wavelength range of approximately 200 to 2500 nm. The developed graphene-covered SMG metasurface further demonstrates a typical feature: the transmittivity of the *P* wave is maximally increased by 10.24% and that of the *S* waves is maximally decreased by 21.84% when a low dc voltage is applied because of the controlled conductive action of the graphene film formed by sequentially stacking 30 layers of single-crystal graphene over the surface of the serrated SMGs. The above behavioral attributes provide an alternative way of realizing the adjustability and controllability of the polarization response characteristics of the incident light wave and performing the fast and fine acquisition of polarization information in polarization imaging.

DOI: 10.1103/PhysRevApplied.21.034062

I. INTRODUCTION

Subwavelength metallic gratings (SMGs), as a typical surface wave excitation architecture [1–3], can effectively converge incident light waves into the ultra-diffraction-limited nanospace to enhance the light reflection or transmission efficacy based on surface-plasmon (SP) resonance [4–8] and Fabry-Perot resonance [9–13]. Their characteristic micro- and nanoscale structural dimensions enable them to exhibit unique light polarization response behaviors that are significantly different from those of conventional gratings [14,15], thus showing promising development prospects in the field of high spatial and radiometric resolution polarization imaging [16,17]. Conventional polarization imaging methods, such as division of time, division of amplitude, division of aperture, and division of the focal plane, are not able to effectively take into account the performance requirements of device integration, light energy utilization efficiency, imaging spatial resolution, and radiometric resolution [18–20]. Because there are still several technical bottlenecks in obtaining polarization image information solely by controlling the spatial arrangement of SMGs [21], the development of new polarization imaging detection architectures and methods has become an urgent need. Considering the case of metallic gratings forming interdigital structures, a primary type of electrical capacitance layout can be designed [22–26]. For example, a typical capacitor can accumulate net charges over the surfaces of two parallel thin electrode plates and, subsequently, the charge density over the surfaces can be easily modulated by varying the applied voltage. Specifically, the intrinsic properties of light-wave reflection or transmission are mainly determined by the surface net charges, including the surface free electrons. So, the incident light-wave response based on a basic capacitive structure can be electrically modulated. In the past few years, SMGs, which can be used to efficiently modulate the surface net charge, such as the free-electron distribution, have been extensively

*x_yzhang@hust.edu.cn

investigated [27–29]. However, there are few studies on the mechanism of light-wave polarization selection or even manipulation using SMGs.

This paper proposes a polarization model based on SP excitation over subwavelength metallic micro-nanostructures from the perspective of the surface net charge, such as the free-electron rearrangement. The incident light waves with initial polarization orientations parallel to the long axis of the grating (parallel waves or *P* waves), which can easily enter the surface of the SMG to excite a relatively intense surface free-electron oscillation and cause a Joule heat loss, are remarkably restrained. Moreover, the incident light waves with initial polarization orientations perpendicular to the long axis of the grating (vertical waves or *S* waves) can be reemitted depending on the resonant nanocavities formed in adjacent nanostrips of the SMGs in the dipole optical antenna mode. A polarized SMG array with four different initial orientations (4*O* SMG) is designed to obtain the desired polarization information simultaneously. Both simulations and experiments of the surface charge arrangement of the 4*O* SMG verify the correctness of the theoretical model. Based on the theory, we construct an interdigital SMG capacitor architecture to adjust the surface charge distribution behavior and modulate the SP mode by powering on to effectively adjust the polarization state as well as the transmission characteristics of near-field and far-field optical waves. By designing the grating with a serrated shape, the surface charges can be pumped to the nanotips, and the tuning of the light-wave polarization response of the metasurface can be improved by modulating the charge arrangement behavior of the tips with larger charge density. Furthermore, the designed graphene-covered serrated grating can change the constraint of the capacitive electric field force on the surface charges into the constraint of the guiding current, which makes the electrical modulation of the polarization response to the incident light waves more significant. Our research lays a foundation for future works, for example, fabricating chessboard SMGs by presenting an arbitrary polarization state arrangement tuned electrically. So, an alternative polarization imaging architecture can be expected by accurately obtaining the needed polarization information of targets through a single exposure of the sensor array.

II. RESULTS AND DISCUSSION

A. Theoretical analysis of surface charge distribution of the SMG

As coupling modes of surface near-field electromagnetic waves and surface free-electron density waves, SPs can be effectively stimulated over a metal-dielectric interface by a relatively strong interaction of photons and electrons. Under the condition of efficient excitation by incident light waves with a suitable frequency, numerous "free electrons" distributed over the surface of a metal structure oscillate forcedly based on the tuning of the incident light waves. On the one hand, electrons are localized around the nanostructure in the form of dipoles, making dipole oscillations called localized surface plasmons (LSPs). Alternatively, they can resonate along the polarization direction of the incident light waves, causing notable surface collective free electrons and thus generating a positively charged microregion following the draining of the free electrons. Owing to the localized spatial alternating arrangement of positive charges and collective free electrons, surface waves composed of surface free-electron density waves and surface near-field electromagnetic waves are stimulated and subsequently diffuse outward; these are surface plasmon polaritons (SPPs). It should be noted that the transmitted surface free-electron density waves are longitudinal waves. The electrons in the excited region are driven by the electric field force of the incident light and the electrons in the nonexcited region are driven by the Coulomb force. Momentum and energy are reflected in the accumulation of the force in time and space, respectively. The transfer of momentum and energy is achieved by transferring photons between electrons [30–33].

Based on this analysis, the polarization response of a metallic nanograting to incident light is studied from the perspective of surface free charge arrangement. A model of coupled surface free electrons and electromagnetic oscillations excited over metal facets by incident light waves possessing the required momentum is shown in Fig. 1. The light fields formed over both the top facet *S*1 and side facet *S*2 of a single metallic nanostrip in the coordinate system are shown in Fig. 1(a), where several representative planes *S*1, *S*2, *S*3, and *S*4 of the grating are labeled, and the first face reached by the light source is referred to as the top facet. The typical charge distributions over the upper and side facets of this metallic nanostrip are shown in Fig. 1(b). Theoretically, the surface electrons on the *S*1 and *S*2 facets will be excited to oscillate by the electric field components parallel to the long axis of the grating (*P* electric field) $\mathbf{E}_y$. The surface charges form a regular positive and negative alternating arrangement following the electromagnetic oscillation mode of the surface wave, with an arrangement period equal to the spatial period of the surface wave, and propagate away from the excitation region to the nonexcitation region in the form of electron density waves, such as the charge clusters extending along the y-axis direction on the *S*1 and *S*2 facets in the figure. The *V*-electric-field component $\mathbf{E}_z$ can oscillate in the nanosized resonant cavity formed by the gap of the adjacent gratings and pass through the SMGs along the wave vector $\mathbf{k}_x$. Positive and negative surface charges will be alternately arranged having been excited by $\mathbf{E}_z$, and the arrangement period is equal to the spatial period of the incident light waves, such as the charges clusters alternately arranged along the x axis on the facet *S*2 in the figure.

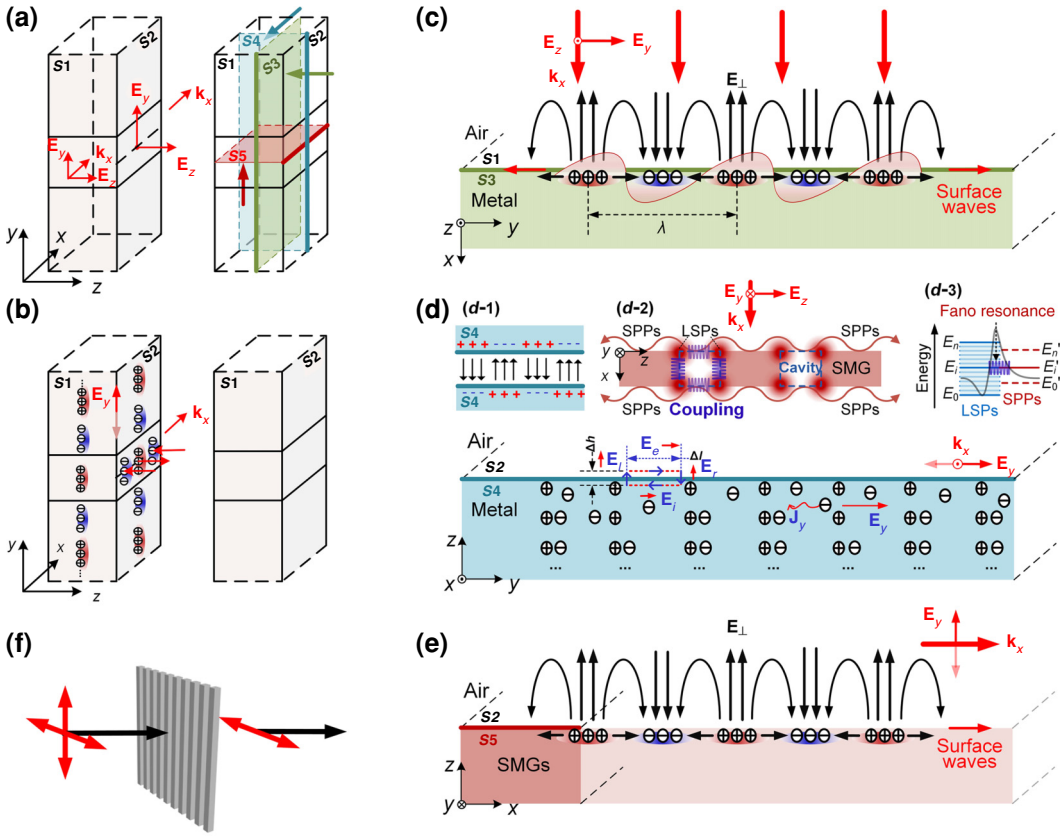

FIG. 1. Diagram showing details of the generation of both surface near-field electromagnetic waves and surface collective oscillations of free electrons excited by light waves with suitable frequency and momentum directly incident on the SMG. (a) Typical polarized electric field components over interfaces of metallic nanostrips of SMG corresponding to incident light waves with wave vector $\mathbf{k}_x$. (b) Charge arrangements over the top interface and sidewall of single nanostrip in the SMG. Colored cross sections and arrows on the right metallic nanostrip indicate three different viewing directions, and reference planes colored in green, blue, and red denote coordinates or spatial position configurations of related interfaces shown in (c)–(e), respectively. (c) Excitation of both near-field electromagnetic waves and surface free electron density waves on facet *S*1. (d),(e) Charge distributions over facet *S*2 stimulated by *P* waves and *S* waves, respectively. Inset (d-1) demonstrates the type of vertical electric field correlation constrained by the coupling of linear dipoles over opposite interfaces between adjacent metallic nanostrips with a subwavelength gap, which is colored in blue. Insets (d-2) and (d-3) illustrate the mode coupling and energy matching of the Fano resonance generated by SMGs. (e) Demonstration of the single dark-red fragment corresponding to the light-red traditional metallic grating with a relatively large depth on the micrometer scale. (f) Typical light-wave polarization orientations for evaluating surface electromagnetic response characteristics of the SMG.

The featured distributions of the electric field components and excited surface charges over selected cross sections of *S*3, *S*4, and *S*5, observed easily from the directions indicated by green, blue, and red arrows, respectively, are shown in Figs. 1(c)–1(e), respectively. The typical distributions of the surface charges stimulated by the $\mathbf{E}_y$ components of the *P* waves with wave vector $\mathbf{k}_x$ and the excited surface electric fields are shown in Fig. 1(c). As presented, $\mathbf{E}_y$ directly passes through facet *S*1 to excite the surface free-electron oscillations. They immediately trigger surface near-field electromagnetic waves and surface free-electron density waves propagating in opposite directions, indicated by two red arrows, over the metal-air interface. This is a forced oscillating mode or even a resonating mode based on the wavelength of the incident light waves, metallic materials, and nanostructure size configuration. The figure presents typical instant electric field distributions over facet *S*1 and near the interface from the interior of the metallic nanostructure. Generally, the excited electric field $\mathbf{E}_\perp$ first reaches a maximum over a small region with a relatively high net positive charge density and subsequently varies its direction or polarity as it approaches adjacent surfaces with net negative charges or electron-accumulating regions.

Figure 1(d) shows the positive and negative charge arrangement in the three-atomic-layer thickness regions on the side of the metallic grating stimulated by the *P* electric field, as well as the coupling of multiple surface plasmon modes. When visible or infrared light waves are incident normally on the nanogap of the nanograting and

subsequently approach the interface labeled $S2$, a loop composed of a square with a width tends to zero at the interface is taken. According to the circuital theorem of the electrostatic field, it is easy to obtain $\mathbf{E}_r = \mathbf{E}_l = 0, \mathbf{E}_e = \mathbf{E}_i$. Therefore, the electric field components parallel to $S2$ can easily penetrate the metallic surface and subsequently stimulate collective free-electron oscillations over the surface. Based on the relation $\mathbf{j}_0 = \sigma \mathbf{E}$, where σ and $\mathbf{j}_0$ are the electrical conductivity and the current density, respectively, the surface free electrons collectively oscillate, stimulated by the incident electric field and propagate away from the excitation region to the nonexcitation region, then form an electron density wave. Part of the energy of the incident light wave is converted into the light wave reflected away from the facet $S2$, and the other part is converted into the kinetic energy of the collective oscillation of the electron density wave on the metal surface. During the collective oscillation of electrons, collisions between electrons or collisions between electrons and the lattice occur, and the kinetic energy is greatly converted into Joule heat to be dissipated.

In general, the energy of the P electric field is almost completely dissipated after the incident light wave enters several atomic layers of the metal surface. That is to say, the P electric field entering the upper surface $S1$ and the side surface $S2$ of the metallic grating will stimulate surface free-electron oscillations and will eventually be completely dissipated. When the gap of the grating is narrow enough, the P electric field entering the gap can be almost completely absorbed by the sidewalls of the gratings. However, considering the air gap of the SMGs at subwavelength scales, the sidewalls of adjacent nanogratings can couple with each other to form dipole optical antennas, which in turn emit relatively strong electromagnetic radiation at the top and bottom of the nanograting. Consequently, this also leads to additional transmission of P waves over the far field. The transmission capacity of P waves shows a tendency for shorter wavelengths to be relatively stronger than longer wavelengths. Theoretically, P waves can be transmitted when the period of the nanograting is comparable with or larger than the incident wavelength. Because the grating gap is relatively large in this case, not all of these P waves can enter the nanograting sidewalls to be completely absorbed. Generally, the incident electric field components perpendicular to $S2$ induce a coupling of the surface charge distributions over the opposite sidewalls of a single nanostrip, and thus cause a vertical electric field coupling correlation to emerge in the nanocavity between adjacent nanostrips, as shown in Fig. 1(d-1). This coupling can be viewed as a dipole antenna originating from the linear dipoles distributed over the opposite sidewalls of the adjacent metallic nanostrips, following which the S waves are transmitted. The transmission is significantly enhanced when the dipoles are localized at the top and bottom of the grating sidewalls because the surface states of the tips formed at the top and bottom corners can accommodate more net charges. This special coupling mode plays a role similar to electromagnetic shielding, to some extent, which weakens the absorption of the P electric field entering the surfaces of the sidewalls of each nanostrip in the SMG.

Under the condition of satisfying the frequency and momentum matching relation over the metallic interface of a single nanostrip, a surface electromagnetic wave field or even SPs can be further excited. The SP modes excited on the cross section of facet $S5$ are shown in Fig. 1(d-2). The incident light interacts with the subwavelength metallic nanograting and generates LSPs at the sharp corners of each nanostrip, and the incident light wave of a specific wavelength also generates SPPs at the top or bottom surfaces of the SMG array. The LSPs at the top or bottom of the adjacent gratings are coupled across the slit, and LSPs at the top and bottom of each grating are also coupled. Incident light waves and surface waves are highly compressed in the nanoslit to form a special cavity mode, and relatively intense antenna radiation is expected to be emitted from both the top and bottom of the nanostrip. The LSP mode localized at the tips of subwavelength metallic structures is not frequency-selective; therefore, the plotted energy model of LSPs is continuous, such as the region covered by blue shading in Fig. 1(d-3), where the typical energy levels E_0, E_i, and E_n are marked with blue lines. Only a specific frequency of the incident light wave can realize wave-vector matching and generate LSP resonance. Meanwhile, the SPP mode with discrete energy levels is excited at the surface of the array structure, and the typical energy levels E_0', E_i', and E_n' are marked with discrete red lines in the figure. When the continuous LSP mode and the discrete SPP mode are superimposed, destructive interference occurs to form an asymmetric Fano resonance line shape. Once the special electromagnetic oscillation mode of Fano resonance is generated, it is accompanied by strong near-field enhancement and abnormal transmission and reflection phenomena.

In the case of a traditional metallic grating with a relatively deep gap, e.g., several tens or even hundreds of microns, the P electric field is almost completely absorbed by the sidewalls of the nanostrip. As for the electric field components vertical to the long axis of the grating (S electric field), notable collective free-electron oscillation excitations can occur over $S2$ along the x axis, as denoted in light red in Fig. 1(e). A resonant waveguide nanocavity is expected in the gap between two opposite nanostrips to transmit the S electric field $\mathbf{E}_z$, along the x-axis direction. The typical polarization propagation through a common metallic grating is shown in Fig. 1(f). For short-wavelength bands, such as the visible region, it is challenging to fabricate nanostructures much smaller

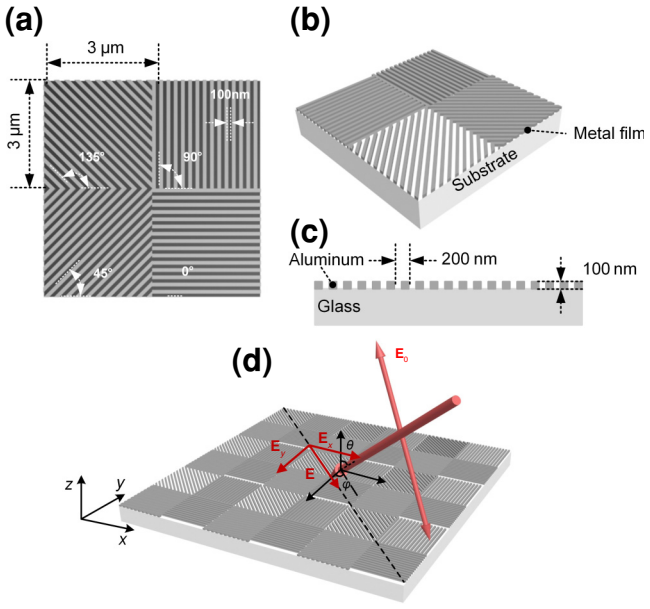

FIG. 2. Structural model of a 4*O* SMG array composed of four nanostrip orientations: 0°, 45°, 90°, and 135°. (a) Critical parameters of each SMG unit, a fragment size of 3×3 μm^2, and metallic nanostrip width and separation of 100 nm. (b) Schematic of the 4*O* SMG unit formed over a common substrate. (c) Cross section profile of SMG on glass substrate fabricated from linear aluminum nanostrip configuration with required period and thickness. (d) Light beams with initial polarized orientation $\mathbf{E}_0$ and incidence angle θ on facet based on the common rectangular coordinate system.

than the grating wavelength because of common technological limitations. At present, metallic grating polarizers are commonly used in the long-infrared band. For visible light and shorter-wavelength bands, new regulatory mechanisms need to be explored in order to achieve the characteristics of desired extinction or tunable polarization response. Owing to the relatively large distinct surface of an SMG, numerous free electrons can be redistributed over it. Specifically, by carefully designing the metallic nanostructures and precisely adjusting the surface energy states of an SMG, the photoelectrical excitation response and subsequently the polarized light wave propagation through the SMG can be effectively manipulated.

B. Numerical simulation of surface charge distribution of the 4*O* SMG

Based on the above theoretical analysis of the characteristic surface charge distribution of SMGs in *P*-wave and *S*-wave excitation, an array structure in which the cells are SMGs with four different polarization orientations is designed. The surface net charge distribution is simulated to visualize the surface charge distribution behavior of SMGs excited by incident light waves with typical polarization angles 0°, 45°, 90°, and 135° to analyze the light-wave polarization response characteristics of the SMGs from multiple polarization angles. The basic structure of the 4*O* SMG is composed of four fragmented SMGs with metallic nanostrip orientations of 0°, 45°, 90°, and 135°, and several key geometric parameters are depicted in Fig. 2. As shown in Fig. 2(a), each SMG unit is constructed by closely arranging four nanogratings of 3×3 μm^2 with the metallic nanostrip orientations mentioned previously; each metallic nanostrip width is 100 nm and the arrangement period is 200 nm. A three-dimensional (3D) view of a 4*O* SMG unit is displayed in Fig. 2(b). The array is fabricated in an aluminum film, which has a high polarization extinction ratio and polarization transmittance, with a thickness of 100 nm, and this film is predeposited on a glass substrate with a thickness of 3 μm. The cross section of the SMG unit is presented in Fig. 2(c). The optical configuration over an incident facet corresponding to polarized light waves $\mathbf{E}_0$, which is expressed in a common rectangular coordinate system shown in black, is illustrated in Fig. 2(d). $\mathbf{E}_x$ and $\mathbf{E}_y$ are the x- and y-direction components of the horizontal projection of the incident light waves $\mathbf{E}_0$. The FDTD method of Lumerical Solutions is used to simulate the efficiency of the 4*O* SMG for controlling light waves. The 4*O* SMG can also be viewed as a type of metasurface for manipulating the distribution of a polarized incident beam and its transmission behaviors. The 4*O* SMG period is set to a typical value of 6 μm based on the periodic boundary conditions in both the x and y directions. First, a beam of plane light waves with a particular polarization orientation is directly incident on a tiny facet or a partial metasurface with an incident angle θ. Subsequently, it is projected over the facet along the black dashed line with a polarized azimuth φ, as shown in Fig. 2(d). Both $\mathbf{E}_x$ and $\mathbf{E}_y$ components can be calculated as $\mathbf{E}_0 \cos\theta \sin\varphi$ and $\boldsymbol{E}_0 \cos\theta \cos\varphi$, respectively, where θ is the angle between the reverse direction of the incident light energy flow vector and the normal of the facet selected.

Considering that the incidence angle θ and polarized azimuth φ of the near-field optical microscope equipment are 45° and the wavelength of the incident beam is 633 nm during the actual measurement process, the simulation model is established based on the measurement configuration described previously to ensure consistency between the simulation and experiment. The main simulation results of the near-field light intensity distribution are shown in Fig. 3. A linear concave-convex-shaped distribution profile of the refractive index crossing each nanostrip of the fragmented 4*O* SMG, which is perpendicular to each nanostrip indicated by the featured orientation mentioned previously, is constructed based on the simulation model, as presented in Fig. 3(a). The yellow arrow represents the electric field projection component **E**. The red nanostrips are aluminum gratings with a real refractive index part of 1.39, and the blue nanolines are air gaps

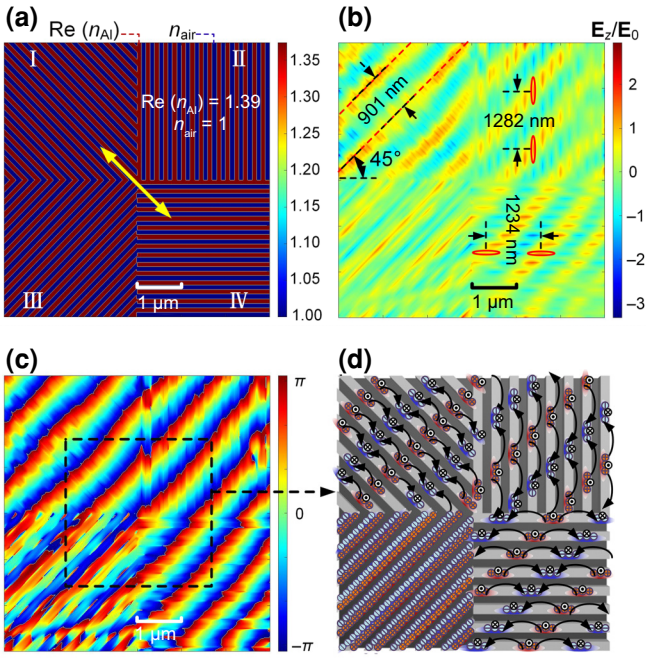

FIG. 3. Near-field light intensity distribution corresponding to the 4*O* SMG unit. (a) Refractive index profile based on the constructed simulation model. The yellow arrow represents the orientation of electric field projection component **E**. Red nanostrips are aluminum gratings with a real refractive index part of 1.39 and blue nanolines are air gaps with a refractive index of 1. (b), (c) z-direction electric field component $\mathbf{E}_z$ and its phase distribution over the top facet of the 4*O* SMG unit. (d) Surface net charge distribution of the 4*O* SMG, where orange microstructures represent net positive charges, blue ones denote net negative charges, and black arrows indicate electric field directions originating from net charges.

with a refractive index of 1. The z-direction components $\mathbf{E}_z$ of the surface electric fields are staggered over the top surface of the 4*O* SMG, as depicted in yellow and green in Fig. 3(b). The direction of the electric field intensity corresponding to the yellow regions is positive, whereas that in the green regions is negative. Surface electric fields are distributed in strips over the entire 4*O* SMG perpendicular to the polarization orientation of **E**. The distances between two adjacent bright orange spots along the different nanograting orientations in regions I, II, and IV are approximately 901, 1282, and 1234 nm, respectively. However, in region III, the electric fields are localized on both sides of each nanostrip. Therefore, an effective wavelength model is established to carefully analyze these phenomena.

First, a light beam illuminates a facet of a 4*O* SMG unit and subsequently propagates between the metal-air-metal interfaces. The excited surface wave propagating along the long axis or the nanostrip orientation of each fragmented SMG is defined as an "effective wave," which can be calculated from the following expressions:

$$\lambda_1 = \frac{\lambda_0}{\sin\theta}, \tag{1}$$

$$\lambda_2 = \frac{\lambda_0}{\sin\theta \sin\varphi}, \tag{2}$$

$$\lambda_4 = \frac{\lambda_0}{\sin\theta \cos\varphi}, \tag{3}$$

where λ_0 is the wavelength of the incident light waves, and the effective wavelengths of the incident light waves along a selected long axis or an orientation of the fragmented SMGs in regions I, II, and IV are λ_1, λ_2, and λ_4, respectively.

Under the condition of the incident wavelength λ_0 being 633 nm, the wavelengths λ_1, λ_2, and λ_4 should be 895, 1266, and 1266 nm, respectively, based on Eqs. (1)–(3). It can be seen that the effective wavelengths approximately match the linear bright spot spacings of around 901, 1282, and 1234 nm, respectively. However, they still present slight deviations of −6, −16, and 32 nm, respectively, corresponding to the light wave vector or the electric field distribution illustrated in Fig. 3(b). The orientations of the short bright spots distributed over the different polarization regions are the same as the given orientations of all fragmented SMGs of the 4*O* SMG unit. Moreover, there is a trend of linear density of the short bright spots having a maximum value in the projection direction of the incident light waves. Linear densities of similar short bright spots are almost equivalent in regions II and IV, and are maximum in region I along the projection direction. The phase distribution of $\mathbf{E}_z$ over the top facet of the 4*O* SMG is shown in Fig. 3(c). The mesophase lines are perpendicular to the polarization orientation of the incident light waves. Therefore, a small central region of the 4*O* SMG unit is magnified to show the surface charge distribution more clearly. It is easy to analyze why the surface electric field intensity forms a nanostrip-shaped distribution corresponding to that exhibited in Fig. 3(b).

In Fig. 3(d), the orange microstructures represent the net positive charges, and the blue ones are the net negative charges. The black arrows indicate the electric field direction of the surface net charges. Based on the surface charges, including the free-electron distribution model established in this study, the surface free electrons can be remarkably excited by the incident polarized light wave and thus oscillate along the incident light-wave polarization orientation. Consequently, the surface net positive charges will also synchronously oscillate, but in the opposite direction to that of the surface free electrons. As shown, the surface free electrons and the corresponding positive charges are arranged alternately along the orientation of the SMG with a period equivalent to the wavelength of the surface wave excitation. The excited electric field

is expected to reach its maximum over the regions with the maximum net positive charge density and subsequently point to the adjacent regions with surface free electron accumulation. In region III, the surface net charges are located on both sides of each nanostrip with a subwavelength width depending on the polarization orientation of the incident light waves. The periodic arrangement of the net positive and net negative charges over the facet of the 4*O* SMG unit can reasonably explain the nanostrip-shaped distribution patterns of the generated surface electric fields, as shown in Fig. 3(b).

C. Near-field measurement of the 4*O* SMG

To verify the theoretical analysis and prediction, a 4*O* SMG with the following specifications is manufactured: nanostrip width 100 nm, period 200 nm, duty ratio 1:1, and nanostrip height 100 nm. First, electron beam evaporation (Ebeam-500S, ALPHA-PLUSCO Ltd., Korea) is conducted to deposit a 100-nm-thick aluminum film on a glass substrate with a thickness of approximately 500 μm. Subsequently, typical electron beam lithography (Vistec EBPG 5000plus ES) is performed to shape a delicate linear micro-nano-structure in a photoresist. Finally, inductively

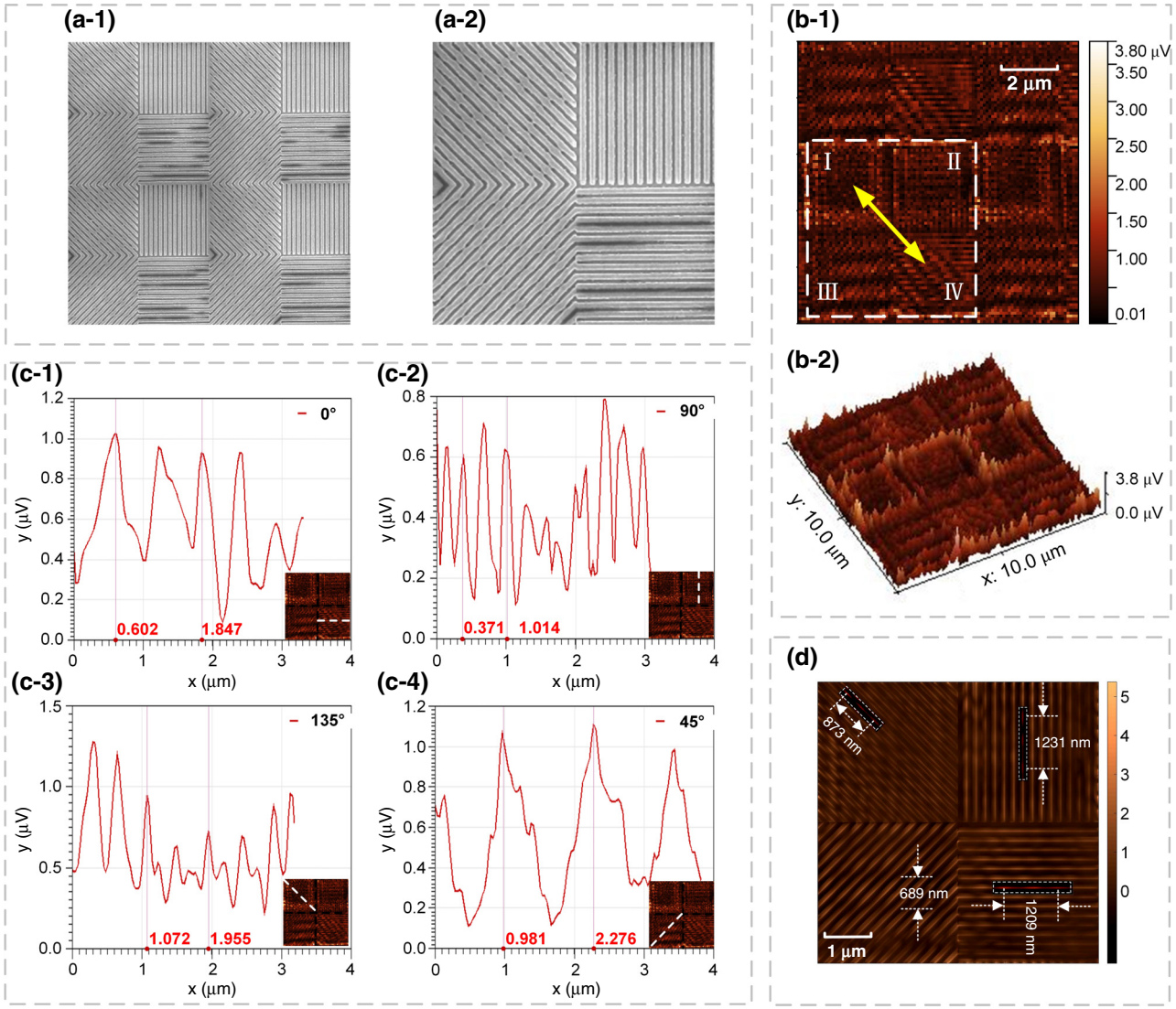

FIG. 4. Typical surface morphology and near-field light-wave intensity distribution of the 4*O* SMG. (a) SEM images of nanostrip arrays with specified four initial orientations (a-1) and 4*O* SMG unit (a-2), which can also be viewed as a metasurface. (b) Near-field light-wave intensity distribution of 4*O* SMG scanned by SNOM according to planform (b-1), in which the 4*O* SMG unit is inside white dashed lines and the yellow arrow points to the projection orientation of incident light waves, and 3D view (b-2). (c) Quantitative measurements of electric field distributions along specific trajectories corresponding to 0° (c-1), 90° (c-2), 135° (c-3), and 45° (c-4) of fragmented SMGs, where scanning is performed along white dashed lines presented in the small insets. (d) The near-field distribution map drawn in MATLAB according to the measured data. After adjusting the image contrast, the dotted boxes mark more evident light spots.

coupled plasma etching (Plasmalab system 100 ICP 180) transfers the formed photoresist nanograting array onto the prefabricated aluminum film. Both the surface morphology and near-field light-wave intensity distribution of the fabricated 4*O* SMG are shown in Fig. 4. A traditional scanning electron microscope is employed to characterize the surface formation of the fabricated 4*O* SMG. Scanning electron microscopy (SEM) images of the arrayed nanostrips with the previously mentioned four initial orientations are shown in Fig. 4(a-1) and a 4*O* SMG unit in a measured sample, which can also be viewed as a metasurface, is shown in Fig. 4(a-2). The near-field optical characteristics of the sample are carefully observed by scattering near-field optical microscopy (SNOM) (NeaSNOM, Quantum Design, Ltd.).

In the experiments, an illuminating laser with a central wavelength of 633 nm is incident obliquely on the surface of an arrayed 4*O* SMG at an incidence angle of 45°. An atomic force microscopy probe (platinum needle) is used to measure the near-field light-wave distribution over the scanning surface based on the initial incident direction, as shown in Fig. 2(d). A noncontacting radar probe is further used to detect the electrical response signals of the near-field light waves over the measured facet of the measured sample. The near-field light wave intensity distribution of the 4*O* SMG is scanned via SNOM, as shown in Fig. 4(b). The planform and 3D view of the measured surface are shown in Figs. 4(b-1) and 4(b-2), respectively, where a 4*O* SMG unit is inside the white dashed lines and the yellow arrow represents the polarization orientation of the projected component of the incident light waves on the sample surface. As shown, the obtained near-field light-wave intensity distribution presents a noticeable repeating regular pattern. There are numerous bright and dark short-line spots, which depend on the initial orientation of each nanostrip cluster. Specifically, the 4*O* SMG can effectively respond to the incident light waves in the visible range. The measured near-field light-wave intensity is scalar, representing a continuously accumulated light-wave energy signal, and the electric field of positive and negative charges is vectorial. So, the bright short-line spots aligned along the SMG in the measured near-field distribution map actually represent an interleaved arrangement of accumulated net positive charges and negative surface free electrons. Because the edges of periodic structures can generate strong localized fields, the edges of regions I and II are both periodic or connected to the ends of periodic structures, so there is a strong near-field signal around these two regions. However, the structures in regions III and IV are misaligned and there is no periodic arrangement, so there is no strong near-field signal generation.

Four typical near-field light-wave intensity curves obtained by scanning the measuring microregions in the four fragmented SMGs with the different initial orientations mentioned previously are shown in Fig. 4(c). The distances between the alternating peaks in the curves corresponding to the different initial orientations of 0°, 90°, and 135° exhibited in Figs. 4(c-1)–4(c-3) are 1245, 643, and 883 nm, respectively. Moreover, the distance between the adjacent peaks corresponding to the local microregion of the 45° orientation in the 4*O* SMG reaches a relatively large value of 1295 nm, which is inconsistent with that of the surface waves predicted from the theoretical calculations. This is because, in addition to the local electric field caused by the aggregation of the surface charges, there is also the electric field generated by the propagating SPP; that is, the near-field signal measured at this wavelength is a superposition of the local and propagating SPP, i.e., the Fano resonance is generated [34–37]. The LSP is a continuous scattering mode, while the SPP is a resonant mode. When the wavelength of the LSP with a periodic structure is close to that of the SPP, Fano resonance occurs, which is typically characterized by asymmetric peaks on the transmittance and reflectivity curves. Therefore, a large shaded region of the surface electric field excitation occurs, particularly in regions I and II in Fig. 4(b), the superposition of different SP modes produces a notable destructive interference effect, and a constructive interference effect is generated in region III. The near-field distribution map is drawn in MATLAB according to the measured data, as shown in Fig. 4(d). It can clearly be seen that the arrangement periods of the net positive and negative charges corresponding to the different orientations of 0°, 90°, and 135° in the SMGs are 1209, 1231, and 873 nm, which are basically consistent with the theoretical prediction. On the surface of the 45° SMG, there are obviously bright and dark nanostripes with a period of 689 nm. It is known that when the periodic grating structure is excited by polarized light in the direction perpendicular to the grating, SPPs will be generated at the specific wave-vector matching condition. For the structure designed in this paper, the wave-vector matching condition is as follows [37]:

$$\mathbf{k}_{\mathrm{SPP}} = \mathbf{k}_0 \sin\theta \pm m2\pi/L, \tag{4}$$

where $\mathbf{k}_{\mathrm{SPP}}$ is the wave vector of the considered SPP mode, $\mathbf{k}_0$ is the wave vector of the incident light, θ is the angle of incidence, m is an integer representing the order of the SPP mode, and L is the period of the 4*O* SMG array. Since the wavelength of the incident light is 633 nm, the light is incident at an angle of 45°, and the array period is 6 μm, taking the order $m = 2$, the wavelength of the excited SPP is 689 nm, which coincides with the nanostripe period of the 45° SMG. Therefore, the microregion III shown in Fig. 4(d) presents notable bright and dark nanostrips, which are formed by the SPPs induced by the SMGs.

Consequently, it can be seen that the constructed SMG with a specific orientation can transmit the *S* waves and absorb the *P* waves to a certain extent. The surface free

electrons driven or resonantly excited by the P waves collectively oscillate along the long axis of the SMG resulting in Joule heat loss, while the S waves transmit through the SMG in the form of dipole radiation by exciting the surface charges of the adjacent nanostrips to generate the dipole oscillation modes. The near-field measurements of 4O SMGs designed already verify the feasibility of the theoretical model regarding the response characteristics of the P waves and S waves on the surface of the nanogratings.

D. Light-wave manipulation of SMGs biased by a dc voltage

In general, the rearrangement and oscillation of the free electrons over the metal surface of an SMG are constrained not only by the incident light waves, but also by the applied bias electric field, which determines the surface free-electron distribution or the aggregation density based on the electric potential formed. Subsequently, a type of periodic slab capacitance structure is also built. Under the action of a negative dc voltage with a gradually increasing amplitude, the surface free-electron distribution density on the local sidewalls of an SMG is expected to increase. Specifically, the number of localized surface free electrons participating in the stimulation in response to P waves increases. While the change of the surface electron density can regulate the dielectric constant of the structure, the imaginary part of the dielectric constant represents the damping term, which is directly related to the efficiency of the conversion of the P waves into heat loss in the form of absorbed damping, and the real part of the dielectric constant represents the polarizability, which directly affects the resonance frequency of the surface plasmons, and consequently affects the transmission and absorption of the S waves [38].

The diagram of the incident light-wave excitation behaviors of the surface net charge distribution over both sidewalls of a pair of metallic nanostrips of an SMG is shown in Fig. 5. The powering approach for driving the basic interdigital SMG is presented in Fig. 5(a), where the SMG sidewall area is s and the adjacent sidewall spacing is d. The surface net charge distributions over the sidewalls of two adjacent metallic nanostrips under the combined action of the applied dc voltage and the incident light waves are shown in Fig. 5(b). In the figure, the accumulated negative and positive charges are denoted in blue and red, respectively. The black arrows represent the electric field formed in the capacitor-shaped architecture. The red arrow indicates the P electric field $\mathbf{E}_y$ of the incident light waves. q_0 denotes a group of excited oscillating electrons. Under the condition of no external interference, the metallic nanostrips should be electrically neutral, and both the free electrons and net positive charges distributed over the facets of the opposite sidewalls are in

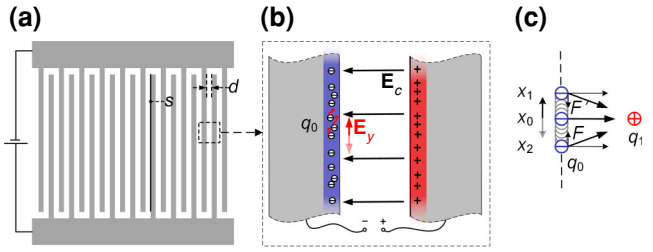

FIG. 5. Modeling diagram of photoelectric excitation of surface net charges distributed over both sidewalls of a pair of metallic nanostrips of an SMG. (a) Basic interdigital SMG architecture powered by a dc voltage. (b) Surface net charge distributions over opposite sidewalls excited by incident light waves and controlled by an applied dc voltage. (c) Surface electron oscillation driven by incident light waves and constrained by the capacitive electric field.

an equilibrium state. Based on the capacitor-shaped architecture, an external power source negatively charges the negative facet, making the other metallic surface positively charged. A relatively stable transient electric field spanning the air gap between the opposite metallic surfaces with a subwavelength distance is expected to be generated that will couple the opposite metallic facets into a nanocavity. Because of the intrinsic vibration of the net charges stimulated by the incident light waves, the pulsing positive and negative charge pairs can also be viewed as types of dipole optical antennas for emitting radiation outside the constructed nanocavity. It should be noted that the surface net charge, including the free-electron oscillations along each nanostrip, which are driven by the P electric field, is strongly constrained by the electric field force. In addition, the surface net charge density is strictly modulated by the electric potential formed between the two metallic facets.

A typical case of constraining a group of oscillating electrons with an amount of electric charge q_0 distributed on a facet is shown in Fig. 5(c). The positive net charge q_1 on the opposite sidewall, which is also bounded by the capacitive electric field force, is also in the same oscillating state. The initial position of the free-electron group q_0 is x_0, and it subsequently oscillates between x_1 and x_2. Its oscillation along the x orientation is restrained by the electric field force F of the positive charge group q_1. The presence of F is expected to affect the frequency and amplitude of the free-electron oscillation mode and to restrain the dipole vibration generated between the opposite facets of each nanocavity discussed, i.e., the dipole radiation is weakened accordingly. Additionally, the P waves entering the interfaces of the sidewalls of each metallic nanostrip of an SMG excite the surface net charge, which involves the surface free-electron oscillation along each metallic nanostrip. Thus, owing to a relatively strong phonon collision resulting from the strong local interaction between

the surface oscillating electrons and the metallic lattice, the incident light energy is converted into Joule heat, which dissipates over the metallic surface of the SMG. The surface net charge density over each metallic nanostrip increases as the applied potential increases, and the greater the number of charges involved in oscillations under parallel wave excitation, the greater the absorption damping, and thus greater Joule heat generation. In summary, applying a voltage not only promotes absorption of P waves, but also suppresses the generation of secondary radiation, so that fewer P waves are transmitted.

Unlike P waves, S waves can effectively excite the SPPs at the surface of the periodic SMG array. In periodic subwavelength metallic nanostrip arrays, SPs can be generated effectively over a metal-dielectric interface. The condition of the incident light-wave frequency matching the plasma frequency of the free-electron gas in a metallic film leads to SP resonance, in which the transmission phenomenon is highly notable. The intrinsic oscillation frequency of the local free electrons excited as mentioned previously can be expressed as $\omega_{\mathrm{p}} = \sqrt{ne^2/\varepsilon_0 m_e}$, where n is the free-electron density, e is the amount of charge of a single electron, ε_0 is the permittivity of free space, and m_e is the effective mass of a surface free electron [39]. When an electric field is generated between two opposite facets in the capacitor-shaped architecture, n is increased, which increases ω_{p} and reduces the SPP wavelength. Moreover, the transmittivity is changed in the frequency band adjacent to the featured frequency point or frequency region. Based on this theoretical analysis, the application of a dc voltage to an SMG to form an electrically tunable capacitor-shaped architecture can be utilized to adjust or even modulate the transmittance of the incident light waves depending on the polarization response behaviors of the SPPs.

As shown, the polarization properties of the SMGs can be easily changed by electrically tuning the electron arrangement. A two-layered functional microstructure composed of a layer of aluminum grating over an infrared glass substrate is designed and fabricated. The typical fabrication process is as follows. A layer of aluminum film of 100-nm thickness is directly grown on the substrate by electron beam evaporation. Subsequently, a pattern is transferred to the aluminum film by electron beam lithography combined with inductively coupled plasma to form a prototype nanograting. The ends of the nanograting are selectively connected to form an interdigital microstructure. The measurements of the electrical adjustment or modulation of the polarization behaviors of the SMGs are shown in Fig. 6. A schematic of the SMGs' light-wave excitation response characteristic measurements is presented in Fig. 6(a). SMGs with a size of 2×2 mm^2 are fabricated with a layer of aluminum film of 100 nm over a glass substrate of approximately 500-μm thickness. A photo of the fabricated nanograting is shown in Fig. 6(b). For the convenience of displaying the full view of the nanograting, the middle part of the grating's long axis is omitted here. The width of each nanostrip of the SMG is 340 nm, and its arrangement period is 600 nm. The measurement light path and the experimental platform for evaluating the polarization behaviors of the electrically controlled SMGs are shown in Figs. 6(c) and 6(d). Because the incident laser is partially polarized, a polarizer is placed behind the laser to form unidirectional polarized beams. Each SMG sample is fixed on a rotatable disc and subsequently shaded to expose only a 2×2 mm^2 area. The electrodes at both ends of the SMGs are connected to a dc supply, and the optical power of the light waves passing through the SMGs is detected using an optical power meter.

Figures 6(e) and 6(f) show the transmission light-wave power of the SMGs irradiated by 633-nm and 2.2-μm lasers before and after being powered by 15 V_{dc}. The electric field profiles in the x-y plane at a vertical polarization incidence are inserted on the right. The red arrow points to the case when charged and the blue arrow points to the case when uncharged. The abscissa in the figures is the angle between the polarization orientation of the incident light waves and the long-axis direction of the nanograting. The incident light waves are approximately parallel to the nanograting at 0° or 180°, and almost perpendicular to the nanograting at 90°. The blue curve in the figures represents the light-wave power variance in the power-off state, whereas the red one denotes that in the power-on state. It can be seen that few P waves are transmitted, whereas many S waves are transmitted when the SMG is in the power-on state. This modulation is much more significant at 633 nm than at 2.2 μm. To explain this phenomenon, the simulated electric field $\mathbf{E}_z$ distribution at a 90° polarization incidence is given in the inset on the right. First, the excitation of incident light at 633 nm is analyzed. Compared with when the power is off, the surface charge distribution area is larger when the power is on, which means that more surface charge is involved in the oscillation and the field enhancement factor is 10 times higher than when the power is off. When excited by 2.2-μm incident light, the situation of the power being on also excites more surface charge, but there is no significant improvement of the field enhancement factor.

The operation of powering on the SMGs requires constructing a capacitor-type architecture, in which the frequency and amplitude of the free-electron oscillation over the local facets of the SMGs are apparently affected by the electric field force between two opposite facets. This remarkably restrains the dipole vibration generated between two opposite facets of each nanocavity; i.e., the dipole radiation, which can be viewed as the origin of the secondary light-wave emission resulting from a dipole optical antenna, is weakened accordingly. Therefore, the

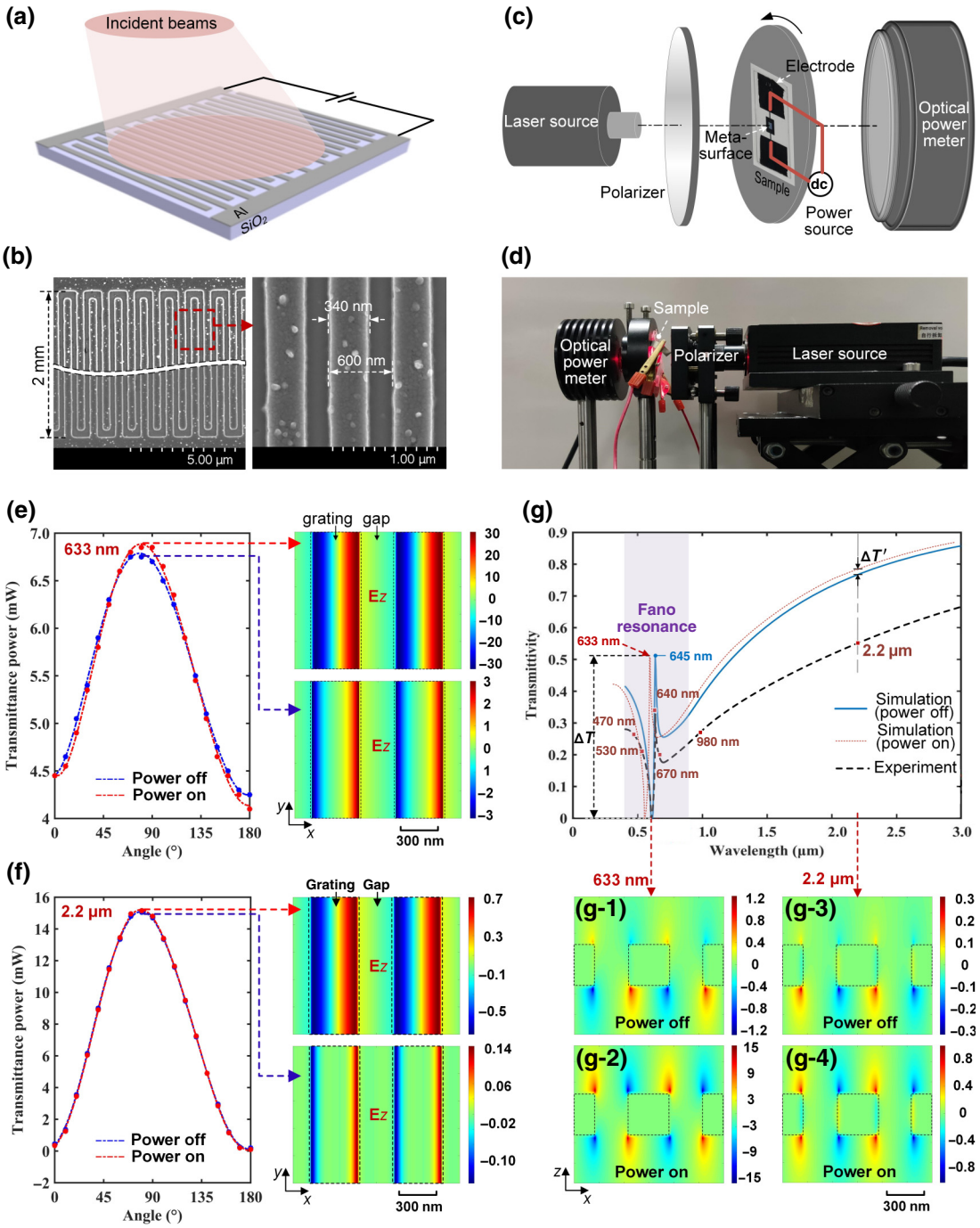

FIG. 6. Measurements of electrical adjustment or even modulation of polarization behaviors of SMGs. (a) Schematic of measurement of light-wave excitation response characteristics of SMGs. (b) Surface topographies of SMGs, where the left side presents the surface morphology of patterned SMGs, and the right side shows an enlarged view of the functional microregion. (c),(d) Measuring the light path and experimental platform for evaluating electrical control of properties of SMGs by applying a dc voltage on SMGs and subsequently testing transmitted light-wave power according to different selected polarization orientations. (e), (f) Transmitted light-wave power of SMGs before and after being powered by 15 V_{dc} signals, illuminated by 633-nm and 2.2-μm lasers. The simulated electric field profiles in the *x*-*y* plane at vertical polarization incidence are inserted on the right. The red arrow points to the case when charged and the blue arrow points to the case when uncharged. (g) The simulation and experiment results of the transmission spectrum of the SMGs excited by *S* waves in a wavelength range from 0.4 to 3 μm, and the discrete red dots represent the experimental data. (g-1),(g-2) Simulated electric field profiles in the *x*-*z* plane before and after the power is turned on, respectively, with a 633-nm laser at a vertical polarization incidence. (g-3),(g-4) The electric field profiles in the *x*-*z* plane before and after the power is turned on, respectively, with a 2.2-μm laser at a vertical polarization incidence.

transmission of the P waves is also reduced in the power-on state. However, the S waves excite the relatively strong SPs on the surface of the nanograting. When an electric field is generated between two opposite facets in the capacitor-shaped architecture, the surface free-electron distribution density n is notably increased, i.e., ω_p is increased and the SP wavelength is reduced. The transmittivity is also changed in the frequency band adjacent to the frequency given previously.

The simulated and experimental results about the transmittivity of the SMGs excited by S waves are shown in Fig. 6(g). Since a continuous spectrum in a wavelength range from 0.4 to 3 μm is not available, six wavelengths of 0.47, 0.53, 0.64, 0.67, 0.98, and 2.2 μm, are selected. The transmittivity is obtained according to the ratio between the transmitted and incident light power: 26.2%, 21.1%, 34.5%, 19.8%, 26.9%, and 55.4%. These data are different from the simulations, but fall on a curve with a similar trend corresponding to the simulation results, verifying the correctness of the simulations. When the incident wavelength λ_0 is 645 nm, there is a peak in the transmittivity, i.e., there is abnormal transmission. There is obvious Fano resonance in the band marked in the purple in the figure. When this special SP mode appears, the electric controlling effect is very significant. The red dashed line in Fig. 6(g) is the simulated transmittivity curve of the power-on case. The SP wavelength—the peak wavelength of the transmittivity curve—generates a blue shift when powered on, causing the transmittivity at the wavelength of 633 nm to significantly increase by ΔT from the trough value of the original Fano curve to the peak value of the current Fano curve. At the wavelength of approximately 2.2 μm, the transmittivity curve is relatively flat, while the transmittivity slightly increases by $\Delta T'$ when the peak wavelength is slightly blue-shifted. Therefore, the transmittivity of the S waves increases in the power-on operation, and an enhancement effect in the visible band can be viewed more notably than in the infrared band. This simply explains why the polarization adjustment or even the modulation effect in the infrared band is worse than in the visible range.

Furthermore, the simulated electric field distribution is used to analyze the behavior of the surface charges by electric control in different bands. The simulated $\mathbf{E}_z$ profiles in the x-z plane at 633 nm (in Fano resonance mode) with vertical polarization incidence are shown in Figs. 6(g-1) and 6(g-2), and the simulated $\mathbf{E}_z$ profiles in the x-z plane at 2.2 μm (not in Fano resonance mode) with vertical polarization incidence are shown in Figs. 6(g-3) and 6(g-4). Among these figures, Figs. 6(g-1) and 6(g-3) are simulations of the power-off state and Figs. 6(g-2) and 6(g-4) are simulations with the power on at a voltage of 15 V_{dc}. As shown, the field enhancement factor increases in the power-on state compared with the power-off state from 1.2 to 15 for 633 nm and from 0.3 to 0.8 for 2.2 μm. At 633 nm in the Fano resonance mode, relatively weak positive and negative dipoles are formed on the upper and lower surfaces of the SMG when it is powered off. When powered on, the charges on the upper surface increase and couple strongly with the charges on the lower surface, resulting in strong dipole radiation and a significant enhancement of the field enhancement factor. For the 2.2-μm not in the Fano resonance mode, the dipole mode is not formed on the upper and lower surfaces of the SMG when it is powered off, and powering on only slightly increases the charge density distributed on the upper and lower surfaces, and the field enhancement factor is not significantly enhanced. It can be seen that the electric control redistributes the surface charge. In particular, in the Fano resonance mode, the charge resonance in the upper and lower surface of SMG is stronger when powered on, resulting in strong dipole radiation.

E. Light-wave regulation by serrated SMGs with adjusted dc voltage

Because the focusing of light over special nanotips can be used to regulate the distribution of the surface net charges stimulated by incident light waves, each flat sidewall in the SMGs described previously is further designed to have a serrated form to more efficiently respond to incident light waves. A diagram of the typical serrated sidewalls in two coupled metallic nanostrips is shown in Fig. 7. The approach for driving the proposed serrated SMGs is presented in Fig. 7(a). The surface net charge distribution over both the serrated sidewalls in two adjacent metallic nanostrips loaded by an adjustable dc voltage is shown in Fig. 7(b). The accumulated negative and positive net charges are shown in blue and red, respectively, and the black arrows represent the electric fields stimulated according to a capacitor-shaped architecture. Through effectively stimulating and driving surface free electrons by an electric field $\mathbf{E}_c$, the surface net charges rapidly gather at the tips, as presented in Fig. 7(c). Generally, the electrons over a typical sidewall are strongly driven by the electric field and then move toward the apexes of the serrated edge. Therefore, the electric field force F acting directly on each electron over the serrated edge can be decomposed into two components vertically and along the local edge, respectively. Consequently, the surface electrons will move according to the electric field component parallel to the surface of the serrated edge, and thus converge at the nearest apex, based on the surface states formed.

It can be expected that when the serrated SMG is powered, the net charges on the opposite facets of two serrated sidewalls will be pumped towards the nearest apexes, and thus apparently enhance the surface density of the net charges gathered at the nanotips. Therefore, a considerable number of net charges will be tightly bound by the nanotips without any response to incident light waves. To

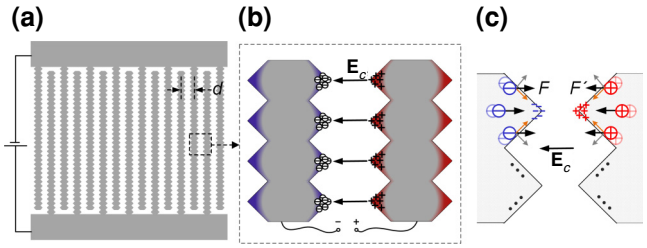

FIG. 7. Diagram of the surface net charge distribution over two opposite serrated sidewalls of two coupled metallic nanostrips in the proposed SMGs. (a) Basic interdigital serrated SMGs powered by an adjusted dc voltage. (b) Surface net charge distribution over two opposite serrated sidewalls also acted on by electric field $\mathbf{E}_c$. (c) Typical rearrangement of the surface net charges near the apexes of two serrated sidewalls controlled according to a capacitive electric field architecture.

the *P* waves, the number of the net charges responding to incident light waves will be decreased, which means that the heat loss originating from the incident light energy conversion will be reduced, resulting in an enhanced light-wave penetration compared with that before powering the SMGs. To the *S* waves, the net charge distributed over the sidewalls will be apparently changed and thus lead to a remarkable variance of the dielectric constant, which means a possibility of modulating the light-wave response behaviors of the developed SMGs.

The morphology of the serrated SMGs and the light-wave transmittance characteristics, which can be modulated by an adjustable dc voltage, are shown in Fig. 8. The serrated SMGs with a size of 2×2 mm^2, which can also be viewed as a kind of metasurface, are fabricated in a layer of aluminum film with 100-nm thickness over a glass substrate with 500-μm thickness, as shown in Fig. 8(a-1). The serrated SMGs are shaped into a basic forked finger form by closely intersecting adjacent fingers in two independent gratings, which are connected directly with two aluminum electrodes. The SEM photograph of the manufactured serrated nanostrips is shown in Fig. 8(a-2). An enlarged view of the functional microregions with typical dimensional parameters is shown in Fig. 8(a-3). The serrated SMGs have a finger period of 600 nm, and the arrangement period of the serrated nanotips on a single nanostrip is 200 nm. The width between two adjacent convex tips is 400 nm, and that between two adjacent concave tips is 200 nm.

A UV-visible-near-infrared spectrophotometer (SolidSpec-3700) is used to measure and evaluate the transmission characteristics of the serrated SMGs according to the *P* waves and *S* waves of the incident light waves in a wavelength range from approximately 200 to 2500 nm, which covers three traditional spectral regions: the UV, visible, and near-infrared. The transmission spectrum corresponding to the *P* waves is demonstrated in Fig. 8(b), in which the transmittivity curves obtained by applying

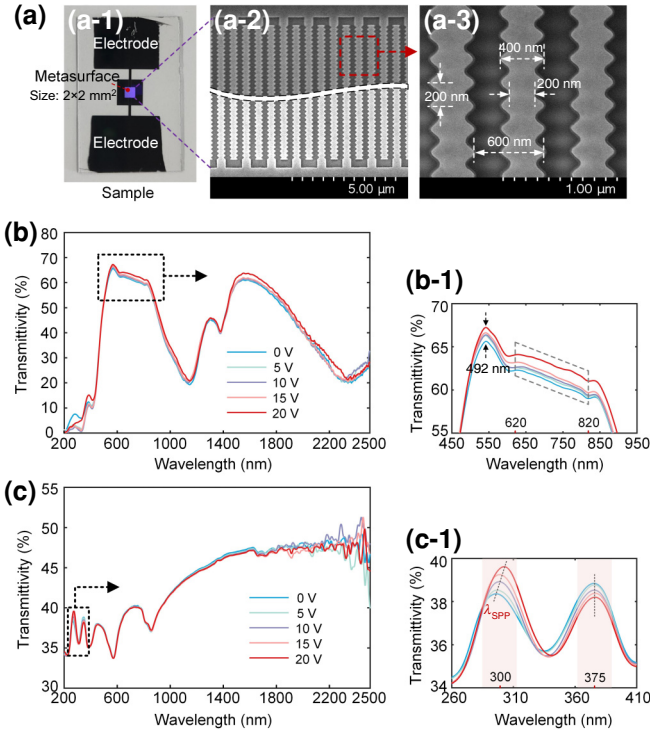

FIG. 8. Morphology of serrated SMGs, which can be modulated by adjusting the applied dc voltage, and its typical light-wave transmittivity characteristics. (a) Serrated SMGs with the required electrical configuration. The sample formed from an aluminum metasurface with two electrodes fabricated over an infrared glass substrate (a-1), its nanostrip-shaped architecture (a-2), and an enlarged view of the serrated microregions with key structural parameters (a-3), are presented. The measured transmission spectra corresponding to the *P* waves (b) and the *S* waves (c) powered by different dc voltages, 0, 5, 10, 15, and 20 V, are given. Enlarged views of the transmittivity curves in typical wavelength ranges from approximately 450 to 950 nm and 260 to 410 nm are shown in (b-1) and (c-1), respectively.

the dc voltages 0, 5, 10, 15, and 20 V, are indicated by blue, green, purple, pink, and red, respectively. Omitting the irregular transmission fluctuation in the low- and high-frequency ends, the intrinsic response behavior of the SMGs is explored only in the wavelength range of 400–2000 nm. As shown, the application of a dc voltage across the sample can obviously enhance the transmittance of *P* waves, and the transmittance tends to increase with the dc voltage. It should be noted that this phenomenon occurs because the surface net charges are almost all pumped onto the nearest apexes and then pinned by an electric field stimulated between two adjacent tips. This decreases the number of net charges that can respond to the *P* waves of the incident light and means that the heat loss from the incident light energy is also reduced; therefore, the transmission of the *P* waves is increased compared with that from before applying the dc voltage. In order to more clearly present the transmittivity variance characteristics,

several enlarged transmittivity curves in a typical spectral band of 450–950 nm are given in Fig. 8(b-1). As shown, a clear peak cluster is located at a wavelength of approximately 492 nm and the transmittivities of 65.64%, 66.32%, 66.43%, 66.67%, and 67.29%, are acquired by applying the dc voltages used previously. Currently, as the dc voltage increases from 0 to 20 V, the transmittivity slightly increases by about 1.65%, and in the wavelength range of 620–820 nm indicated by a dashed box, the transmittivity also demonstrates a significant variance with an increment of approximately 2.2%.

The measured transmission spectra of the SMGs corresponding to the *S* waves are shown in Fig. 8(c), where the transmittivity curves obtained by applying the same dc voltages used previously are shown in blue, green, purple, pink, and red, respectively. As shown, the transmittivity variance is more significant in the wavelength band of 260–410 nm indicated by a dashed box, and an enlarged view is given in Fig. 8(c-1). The transmittivity peak wavelength near 300 nm presents a rightward trend from an initial 295.98 nm to the slightly different values of 297.04, 298.49, 299.62, and 302.57 nm, as the dc voltage is gradually increased from 0 to 5, 10, 15, and 20 V, respectively. The peak transmittivity also exhibits an increasing trend as the voltage increases in a sequence of 38.40%, 38.56%, 38.95%, 39.29%, and 39.66%, with a similar transmittivity increment of approximately 1.26%. Considering that the period of the serrated SMGs is 600 nm, which will lead to an excited SPP with a wavelength λ_{SPP} of approximately 300 nm, a resonance peak should be at a wavelength of around 300 nm. As the applied voltage gradually increases, more surface free electrons are pumped onto the apexes, and thus the surface electron or the net positive charge density n away from the apexes decreases. According to the relation $\omega_p = \sqrt{ne^2/\varepsilon_0 m_e}$, ω_p should decrease and the wavelength λ_{SPP} increase, which is the reason for the rightward shift of the resonance peak mentioned previously. In addition, a higher electron density at the apex of each nanotip will make the dipole resonance more intense, resulting in an increase in the resonance peak with increasing voltage. It should be noted that the peak transmittivities at a typical nonresonant wavelength of around 375 nm show a total drop of 0.64% through the sequence 38.88%, 38.81%, 38.57% 38.42%, and 38.24%, as the voltage applied is increased, while the peak wavelength is almost constant. This phenomenon should be attributed to the fact that a larger voltage will provide a larger capacitive electric field to bind the tip's positive-negative charge pair, and thus remarkably weaken the dipole oscillation that generates secondary radiation, which means an apparent decrease in the transmittivity of the *S* waves.

Considering that graphene has excellent electrical and optical properties, such as high carrier mobility, high thermal conductivity, and high nonlinear coefficient, a graphene-covered serrated SMG metasurface is further developed to study its response to incident light waves. The physical model is formed by directly covering the surface of the serrated SMGs with a graphene film formed by sequentially stacking 30 layers of single-crystal graphene, as shown in Fig. 9(a). The serrated SMG metasurface made of aluminum is backed by a silica substrate. The SMGs are arranged as forked fingers, with each end connected to aluminum electrodes, which are then powered by an external dc power source. The inset shows an enlarged 3D structural model in detail, with the physical model of graphene clearly demonstrated. The graphene film is on top of the serrated SMG metasurface.

With the dc power source operating, the adjacent serrated SMGs exhibit charged features with opposite polarity. A schematic diagram of the surface net charge movement driven by a reverse dc voltage applied over the adjacent nanostrips is depicted in Fig. 9(b). In this figure, the gray pattern represents a serrated unit of the SMG, and the purple honeycomb lattice connecting adjacent nanostrips indicates a graphene film. Under the action of an external dc voltage, the tips of adjacent nanostrips are charged with opposite polarity, and the positive and negative polarities are marked in red and blue in the figure. Once powered on, the surface net charges stimulated by the incident light waves will converge at the apexes. Depending on the magnitude of the external voltage, the electrons at the tips of the serrations are transferred through the graphene layer to varying degrees to form a conductive current. The number of electrons in the graphene layer to some extent indicates the magnitude of the current generated. The electrons transferred away from the negatively charged serrations are marked with gray shading. The higher the applied dc voltage, the larger the conductive current that is formed in graphene, meaning more electrons are transmitted through the graphene layer. That is to say, the number of charges remaining on the surface of the serrated grating is remarkably affected by the current going through the graphene dielectric layer, which can be viewed as a controlling factor because of the graphene's conduction ability being restricted or even adjusted by the dc voltage bias. By gradually increasing the voltage from the initial 5 V to the final 20 V in increments of 5 V, it can be expected that more net charges joining a directional movement will signify a relatively larger current. For example, the measured current goes from the initial 1.78 to 3.65 to 5.52 mA to the final 7.55 mA. This behavior is obviously different from that of the serrated SMGs without a graphene covering, whose net charge distribution over the apexes is only constrained by the capacitive electric field.

The measured transmission spectra of the graphene-covered serrated SMGs corresponding to both the *P* waves

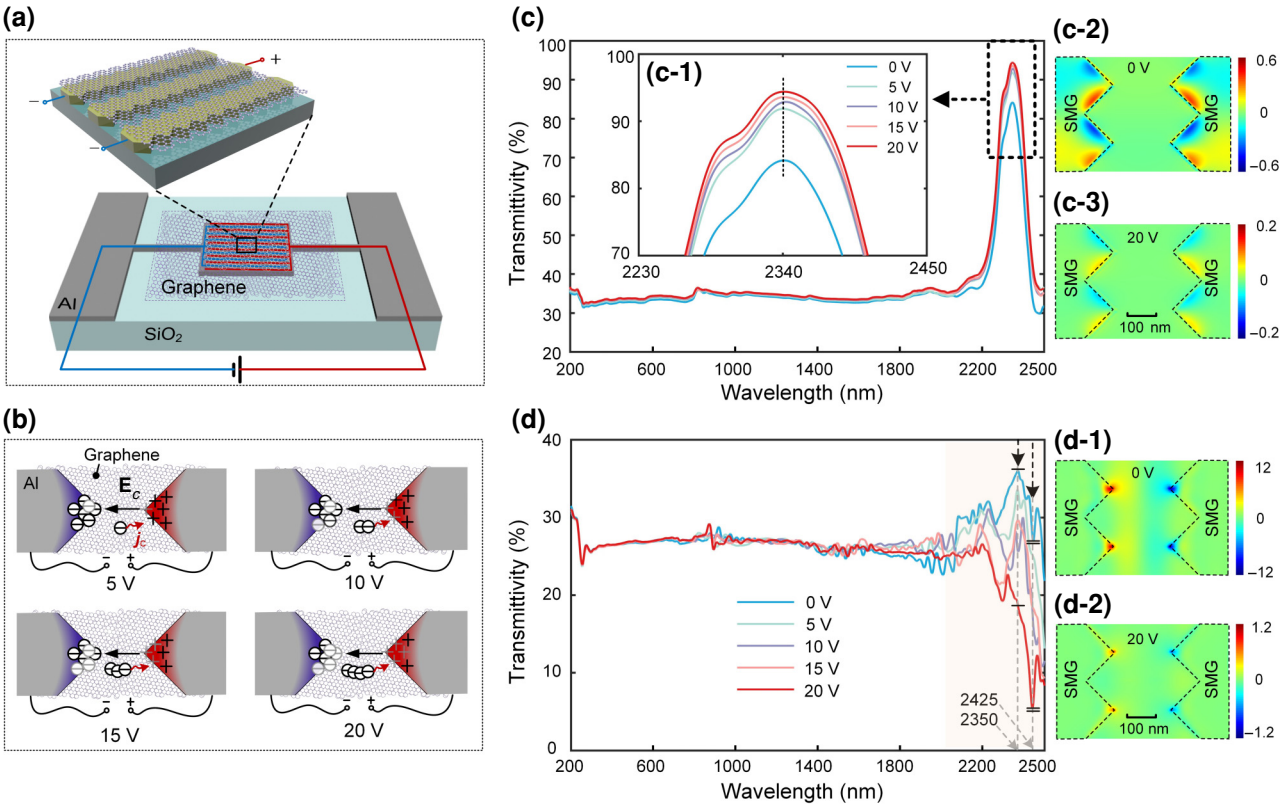

FIG. 9. Changing the transmission behaviors of the graphene-covered serrated SMGs by electrically adjusting or even modulating for the manipulation of the *P* waves and *S* waves. (a) The fabricated graphene-covered serrated SMGs powered by a reversed dc voltage. (b) Typical net charge arrangement and their short transportation over the serrated nanostrips through the graphene film biased by a dc voltage of 5, 10, 15, and 20 V. (c) Measured transmission spectra corresponding to the *P* waves powered by the same dc voltage. (c-1) An enlarged view of the transmittivity curves in a featured subband. The simulated electric field profiles on the upper surface of the graphene-covered serrated SMGs when powered by a 0 V dc voltage in (c-2) and 20 V in (c-3). (d) Typical measured curves by electrically tuning the *S* waves. The simulated electric field profiles on the upper surface of the graphene-covered serrated SMGs when powered by a 0 V dc voltage in (d-1) and 20 V in (d-2).

and *S* waves are shown in Figs. 9(c) and 9(d). The simulated electric field profiles on the upper surface of the serrated SMGs when powered by 0 and 20 V dc voltages are inserted on the right. The measured curves at dc voltages of 0, 5, 10, 15, and 20 V are colored blue, green, purple, pink, and red, respectively. Compared with the serrated SMGs described previously, the graphene-covered samples generally demonstrate a lower transmittance. However, an anomalous transmission window can be observed in the wavelength region of 2.2–2.5 μm, which is related to a strong dipole resonance owing to a strong coupling between the serrated nanostrips and graphene layer. As shown, the application of a dc voltage biasing across the graphene-covered sample remarkably enhances the transmittance of the *P* waves. A significant transmission peak cluster occurs at the central wavelength of approximately 2340 nm, as shown in an enlarged view in the inset of Fig. 9(c). The near-infrared transmittance will slightly rise with increasing dc voltage from the initial 0 V to the final 20 V in increments of 5 V corresponding to the measured values of 84.36%, 92.05%, 93.04%, 93.67%, and 94.60%.

Typical cases of 0 and 20 V dc voltage are selected to simulate the electric field distribution on the upper surface of the serrated SMG, to demonstrate the response of the graphene-covered serrated SMG metasurface to the *P* wave. The simulated electric field profiles with an incident wavelength of 2340 nm are shown in Figs. 9(c-2) and 9(c-3). As shown in Fig. 9(c-2), when the serrated SMG is not powered on, a large number of charges are distributed at the edge of the serrated SMG sidewalls, and when the external dc voltage is 20 V, the charges distributed at the edge of the serrated SMG sidewalls decrease, as shown in Fig. 9(c-3). This is precisely because once the adjacent serrated SMGs are powered on, the charges converging at the sidewall edges can be transmitted through the graphene layer to form a current. Moreover, the higher the applied dc voltage, the higher the transport current formed in the graphene, and so more electrons are transported through

the graphene layer and fewer charges remain at the sidewall edges. It can be expected that when the *P* waves effectively drive the surface net charge oscillation along a zig-zag surface, fewer accumulated charges remain on the serrated SMG surface, resulting in a relatively weak Joule heat loss, which is why a higher applied dc bias voltage leads to higher transmittance for *P* waves.

The measured transmission spectra and the simulated electric field profiles corresponding to the *S* waves are depicted in Fig. 9(d). As shown, the transmittivity has a relatively stable value of approximately 26% in the wavelength range of 200–1800 nm, which covers UV, visible, and near-infrared regions, and then vibrates strongly once the wavelength exceeds approximately 1800 nm, thus exhibiting an obviously different variance trend to that of the *P* waves. It is noted that the transmittivity at a typical wavelength of 2350 nm decreases from around 36.12% at 0 V to around 18.60% at 20 V. The vibrating range of the transmittivity curves is more than a typical extent of approximately 17.52%. The transmittivities at another typical wavelength of approximately 2425 nm also decreases by 21.48% from the initial value of around 26.91% at 0 V to the final value of about 5.43% at 20 V. The simulated electric field distributions of the metasurface excited by the *S* waves at an incident wavelength of 2350 nm are shown in Figs. 9(d-1) and 9(d-2). As shown in Fig. 9(d-1), when the serrated SMG is not powered on, a large number of charges are distributed at the tips. Moreover, when the external dc voltage is 20 V, the graphene layer will transfer charges, reducing the charges distributed at the tips, as shown in Fig. 9(d-2). These transmittivity shifts are attributed to a confinement effect of the surface net charges extracted to join the current in the graphene film. That is to say, the conductive current formed by charge transfer in the graphene film reduces the number of charges originally converging at the SMG tips, and consequently suppresses the electric-dipole oscillation between opposite serrated sidewalls. This effect can be adjusted or modulated by the dc bias voltage; therefore, a higher applied dc bias voltage leads to a lower transmittance for the *S* waves of the graphene-covered serrated SMG metasurface.

III. CONCLUSION

In this paper, a surface charge manipulation approach based on surface-plasmon excitation and adjustment effects by SMGs is proposed. It is shown that surface free electrons can be effectively excited by incident light waves with different initial polarization orientations and subsequently redistributed, thus producing ordered and strong oscillations. A polarized SMG array with four different initial orientations (4*O* SMG) of 0°, 45°, 90°, and 135° is designed and fabricated; its near-field measurements verify the critical theoretical predictions about the ordered distribution of free electrons on the SMG surface. The developed SMG can also be viewed as a type of metasurface with patterned fine micro-nano-structures in which the Fano resonance mode can be effectively excited in the wave-vector matching condition over the constructed nanograting. Based on theory, an interdigital capacitor structure is constructed, which aims to modulate the Fano resonance mode by electrically modulating the charge arrangement, thus effectively manipulating the polarization and transmission characteristics of the light waves. By shaping the serrated sidewalls and further covering the fabricated SMGs with a graphene film, the surface net charges accumulating at the nearest apexes of the nanotips can be more efficiently electrically controlled to clearly enhance or suppress the penetration of incident light waves. This research promotes the rapid acquisition of polarization information in polarization imaging.

ACKNOWLEDGMENTS

The authors acknowledge the financial support from National Natural Science Foundation of China (Grant No. 61176052). The authors would like to thank Fangfang Peng, Xiuxia Wang, Yizhao He, and Xiaolei Wen from the University of Science and Technology of China for process support, and thank Tiantian Zeng of the Analytical and Testing Center of Huazhong University of Science and Technology for providing the testing equipment.

[1] I. Jung, M. Kim, K. Min, G. Kim, M. Jang, M. K. Sang, D. J. Park, and S. Park, Surface plasmon resonance extension through two-block metal-conducting polymer nanorods, Nat. Commun. **9**, 1 (2018).

[2] S. Raza, N. Stenger, A. Pors, T. Holmgaard, S. Kadkhodazadeh, J. B. Wagner, K. Pedersen, M. Wubs, S. Bozhevolnyi, and N. Mortensen, Extremely confined gap surface-plasmon modes excited by electrons, Nat. Commun. **5**, 4125 (2014).

[3] Y. Liang, K. Koshelev, F. C. Zhang, H. Lin, S. R. Lin, J. Y. Wu, B. H. Jia, and Y. Kivshar, Bound states in the continuum in anisotropic plasmonic metasurfaces, Nano. Lett. **20**, 6351 (2020).

[4] Q. Shang, Z. Shuai, C. Jie, P. Yang, and Q. Zhang, Surface plasmon enhanced strong exciton-photon coupling in hybrid inorganic-organic perovskite nanowires, Nano Lett. **18**, 6 (2018).

[5] C. Y. Cho and S. J. Park, Enhanced optical output and reduction of the quantum-confined Stark effect in surface plasmon-enhanced green light-emitting diodes with gold nanoparticles, Opt. Express **24**, 7488 (2016).

[6] H. Huang, F. Wang, Y. Liu, S. Wang, and L. M. Peng, Plasmonic enhanced performance of an infrared detector based on carbon nanotube films, ACS Appl. Mater. Interfaces **9**, 12743 (2017).

[7] M. Pu, X. Ma, X. Li, Y. Guo, and X. Luo, Merging plasmonics and metamaterials by two-dimensional subwavelength structures, J. Mater. Chem. C **10**, C7TC00440K (2017).

[8] J. Liang, L. Y. Ren, H. J. Ju, E. S. Qu, and Y. L. Wang, Visibility enhancement of hazy images based on a universal polarimetric imaging method, J. Appl. Phys. **116**, 173107 (2014).
[9] S. Yi, Q. Lin, Z. Xiang, X. Luo, and L. L. Wang, Controlling terahertz surface plasmon polaritons in Dirac semimetal sheets, Opt. Mater. Express **8**, 884 (2018).
[10] Y. T. Chen and Y. F. Chen, Enhanced random lasing in ZnO nanocombs assisted by Fabry-Perot resonance, Opt. Express **19**, 8728 (2011).
[11] Y. Tian, Z. Guo, Z. Liu, H. Lin, X. Li, J. Chen, S. Deng, and F. Liu, Efficiently enhanced the visible-light absorption of monolayer WS2 by constructing an asymmetric Fabry-Perot cavity, Mater. Today Nano **14**, 100112 (2021).
[12] M. Jiang, C. Miao, H. Xu, J. Ji, and C. Kan, Employing rhodium tripod stars for ultraviolet plasmons enhanced Fabry-Perot mode lasing, CrystEngComm **22**, 5578 (2020).
[13] S. Shu, C. Huang, M. Zhang, and Y. Yan, Greatly enhanced electric field by the improved metal-insulator-metal structure in the visible region, Nanotechnology **30**, 32LT01 (2019).
[14] D. Crouse and P. Keshavareddy, Role of optical and surface plasmon modes in enhanced transmission and applications, Opt. Express **20**, 7760 (2005).
[15] Q. Li, Z. Li, H. Yang, H. Liu, X. Wang, J. Gao, and J. Zhao, Novel aluminum plasmonic absorber enhanced by extraordinary optical transmission, Opt. Express **24**, 25885 (2016).
[16] H. Zhang, B. Abhiraman, Q. Zhang, J. S. Miao, K. Y. Jo, S. Roccasecca, M. Knight, A. Davoyan, and D. Jariwala, Hybrid exciton-plasmon-polaritons in van der Waals semiconductor gratings, Nat. Commun. **11**, 3552 (2020).
[17] R. Ji, C. Jin, K. Song, S. Wang, and X. Zhao, Design of multifunctional Janus metasurface based on subwavelength grating, Nanomaterials **11**, 1034 (2021).
[18] E. Otte, K. Tekce, S. Lamping, B. J. Ravi, and C. Denz, Polarization nano-tomography of tightly focused light landscapes by self-assembled monolayers, Nat. Commun. **10**, 1 (2019).
[19] E. Engay, D. Huo, R. Malureanu, A. I. Bunea, and A. Lavrinenko, Polarization-dependent all-dielectric metasurface for single-shot quantitative phase imaging, Nano Lett. **21**, 3820 (2021).
[20] O. Reshef, M. DelMastro, K. Bearne, A. Alhulaymi, L. Giner, R. Boyd, and J. Lundeen, An optic to replace space and its application towards ultra-thin imaging systems, Nat. Commun. **12**, 3512 (2021).
[21] S. Park, G. Lee, S. H. Song, C. H. Oh, and P. S. Kim, Resonant coupling of surface plasmons to radiation modes by use of dielectric gratings, Opt. Lett. **28**, 1870 (2003).
[22] S. Cakmakyapan, P. K. Lu, A. Navabi, and M. Jarrahi, Gold-patched graphene nano-stripes for high-responsivity and ultrafast photodetection from the visible to infrared regime, Light Sci. Appl. **7**, 173 (2018).
[23] N. Liu and Y. Gao, Recent progress in micro-supercapacitors with in-plane interdigital electrode architecture, Small **13**, 45 (2017).
[24] J. Pu, X. Wang, T. Zhang, S. Li, J. Liu, and K. Komvopoulos, High-energy-density, all-solid-state micro-supercapacitors with three-dimensional interdigital electrodes of carbon/polymer electrolyte composite, Nanotechnology **27**, 045701 (2016).
[25] J. Liu, J. Du, J. Wang, and J. Yang, Long thickness-extensional waves in thin-film bulk acoustic wave filters affected by interdigital electrodes, Ultrasonics **75**, 226 (2017).
[26] Q. Zhang, L. Huang, Q. Chang, W. Shi, L. Shen, and Q. Chen, Gravure-printed interdigital micro-supercapacitors on a flexible polyimide substrate using crumpled graphene ink, Nanotechnology **27**, 105401 (2016).
[27] C. Ma, S. Kim, and N. X. Fang, Far-field acoustic subwavelength imaging and edge detection based on spatial filtering and wave vector conversion, Nat. Commun. **10**, 204 (2019).
[28] T. H. Tsai, X. Yuan, and D. J. Brady, Spatial light modulator-based color polarization imaging, Opt. Express **23**, 11912 (2015).
[29] J. Yang, S. Qiu, W. Jin, X. Wang, and F. Xue, Polarization imaging model considering the non-ideality of polarizers, Appl. Opt. **59**, 306 (2020).
[30] Z. Mamiyev and H. Pfnür, View on Si(111)-(5×2)-Au with plasmon spectroscopy, Phys. Rev. B **102**, 075438 (2020).
[31] T. Lichtenstein, Z. Mamiyev, E. Jeckelmann, C. Tegenkamp, and H. Pfnür, Anisotropic 2D metallicity: Plasmons in Ge(100)-Au, J. Phys.: Condens. Matter **31**, 175001 (2019).
[32] Z. Mamiyev, M. Tzschoppe, C. Huck, A. Pucci, and H. Pfnur, Plasmon standing waves by oxidation of Si(553)-Au, J. Phys. Chem. C **123**, 9400 (2019).
[33] M. Tzschoppe, C. Huck, F. Hotzel, B. Gunther, Z. Mamiyev, A. Butkeyich, C. Ulrich, L. H. Gade, and A. Pucci, How adsorbates alter the metallic behavior of quasi-1D electron systems of the Si(553)-Au surface, J. Phys.: Condens. Matter **31**, 195001 (2019).
[34] Y. Zhang, Y. R. Zhen, O. Neumann, K. Jared, N. Peter, and J. Naomi, Coherent anti-Stokes Raman scattering with single-molecule sensitivity using a plasmonic Fano resonance, Nat. Commun. **5**, 4424 (2014).
[35] K. L. Litvinenko, N. H. Le, B. Redlich, C. R. Pidgeon, N. V. Abrosimov, Y. Andreev, Z. Huang, B. N. Murdin, *et al.*, The multi-photon induced Fano effect, Nat. Commun. **12**, 454 (2021).
[36] M. Limonov, M. Rybin, A. Poddubny, and Y. Kivshar, Fano resonances in photonics, Nat. Photon. **11**, 543 (2017).
[37] R. Nicolas, G. Lévêque, J. Marae-Djouda, G. Montay, Y. Madi, J. Plain, Z. Herro, M. Kazan, P. Adam, and T. Maurer, Plasmonic mode interferences and Fano resonances in metal-insulator-metal nanostructured interface, Sci. Rep. **5**, 14419 (2015).
[38] A. Alabastri, M. Malerba, E. Calandrini, A. Manjavacas, F. D. Angelis, A. Toma, and R. P. Zaccaria, Controlling the heat dissipation in temperature-matched plasmonic nanostructures, Nano Lett. **17**, 5472 (2017).
[39] L. L. Yu, Y. Zhao, L. J. Qian, M. Chen, S. M. Weng, Z. M. Sheng, D. A. Jaroszynski, W. B. Mori, and J. Zhang, Plasma optical modulators for intense lasers, Nat. Commun. **7**, 11893 (2016).